Microfluidics and Nanofluidics (2018) 22:36
https://doi.org/10.1007/s10404-018-2056-2

RESEARCH PAPER

Effects of geometry factors on microvortices evolution in confined square microcavities

Feng Shen[1,2] · Min Xu[1] · Bin Zhou[3] · Zheng Wang[1] · Zhaomiao Liu[1]

Received: 26 November 2017 / Accepted: 7 March 2018 / Published online: 13 March 2018

Abstract

Recently, microcavities have become a central feature of diverse microfluidic devices for many biological applications. Thus, the flow and transport phenomena in microcavities characterized by microvortices have received increasing research attention. It is important to understand thoroughly the geometry factors on the flow behaviors in microcavities. In an effort to provide a design guideline for optimizing the microcavity configuration and better utilizing microvortices for different applications, we investigated quantitatively the liquid flow characteristics in different square microcavities located on one side of a main straight microchannel by using both microparticle image velocimetry (micro-PIV) and numerical simulation. The influences of the inlet Reynolds numbers (with relatively wider values $Re=1$–400) and the hydraulic diameter of the main microchannel ($D_H=100$, 133 µm) on the evolution of microvortices in different square microcavities (100, 200, 400 and 800 µm) were studied. The evolution and characteristic of the microvortices were investigated in detail. Moreover, the critical Reynolds numbers for the emergence of microvortices and the transformation of flow patterns in different microcavities were determined. The results will provide a useful guideline for the design of microcavity-featured microfluidic devices and their applications.

Keywords Microfluidics · Microcavity · Microvortices · Flow pattern · Microparticle image velocimetry (micro-PIV)

1 Introduction

Microfluidics of lab-on-a-chip systems have developed rapidly in last decade in multidisciplinary research fields (Utada et al. 2005; Whitesides 2006; Sackmann et al. 2014), such as physics, biology, chemistry, material science, and fluid mechanics (Lindström and Andersson-Svahn 2010; Mu et al. 2013; Huang et al. 2017; Lin et al. 2017; Niu et al. 2011). Taking advantage of flow characteristics in microscale, microfluidics can be characterized as the science and technology of manipulating and controlling fluids in microfluidic devices (Stone et al. 2004; Baroud et al. 2010). The fine and precise control of fluid flows in microfluidic devices is highly demanded in different applications. To meet the demand, diverse microfluidic devices with different configurations have been developed. It is significantly important to understand thoroughly the flow behaviors in the microfluidic devices (Bremond et al. 2008; Skelley et al. 2009; Anna 2016; Amini et al. 2014; Zhang et al. 2016).

Recently, microcavities have become an integral part of diverse microfluidic devices in many microfluidic applications, for example controlling of the coalescence of microdroplets (Tan et al. 2004; Baroud et al. 2010; Shen et al. 2017a, b), trapping of microdroplets (Wang et al. 2009) and cell culture (Yew et al. 2013; Luo et al. 2008; Liu et al. 2008; Vrhovec et al. 2011). Various microcavity geometric configurations have been developed, for example microwells (Cioffi et al. 2010; Hur et al. 2010; Jang et al. 2011) and microgrooves (Khabiry et al. 2009; Park et al. 2010; Khabiry et al. 2009) located on the bottom of the microchannel for

Electronic supplementary material The online version of this article (https://doi.org/10.1007/s10404-018-2056-2) contains supplementary material, which is available to authorized users.

✉ Feng Shen
shenfeng@bjut.edu.cn

1 College of Mechanical Engineering and Applied Electronics Technology, Beijing University of Technology, Beijing 100124, China

2 Beijing Key Laboratory of Advanced Manufacturing Technology, Beijing University of Technology, Beijing 100124, China

3 College of Civil Engineering and Architecture, Weifang University, Weifang 261061, China

cell trapping and culture, and microcavities with square (Yu et al. 2005), rectangular (Yew et al. 2013), cylinder (Fishler et al. 2013; Tenenbaumkatan et al. 2015), diamond (Chiu 2007; Shelby et al. 2003), and trapezoid (Fan et al. 2014) shapes located on the side of microchannels in many microfluidic applications. Yet, to design successfully the microfluidic devices featuring microcavities, it is important to select well-defined geometries and understand the characteristic of the microvortices thoroughly (Fishler et al. 2013; Shen et al. 2015). Among the existing choices of microcavity geometries, the rectangular shape is the most common configuration as its advantage in an important application of cell or particle high-throughput sorting (Hur et al. 2011; Mach et al. 2011; Park et al. 2009; Zhou et al. 2013; Khojah et al. 2017). However, the above-reported microcavities of different configurations were designed mainly by experience, and the fluid flow behaviors in the microcavities determined by inlet Reynolds number (*Re*) and the microcavities geometry have not been thoroughly studied.

The main reason for the increasing use of microcavities in microfluidics is that microcavities can be used to control the formation of microvortices (Shelby et al. 2003; Chiu 2007). The operating principle of several microfluidic devices is based on the creation of microvortices (Karimi et al. 2013; Sajeesh and Sen 2014; Haller et al. 2015). Flow in microcavities can be characterized by flow separation and internal recirculation or microvortices (Yu et al. 2005; Fishler et al. 2013), which have been proved to be a versatile and powerful tool in microfluidics (Amini et al. 2014; Zhang et al. 2016). In particular, microvortices have been utilized for single-cell manipulation (Shelby et al. 2004; Chiu 2007), rare cells enrichment (Khojah et al. 2017; Hur et al. 2011; Sollier et al. 2014), particle focusing, sorting and trapping (Park et al. 2009; Wang et al. 2013; Hsu et al. 2008; Zhou et al. 2013; Petit et al. 2012), on-chip microcentrifuges (Mach et al. 2011; Pertaya-Braun et al. 2011), plasma extraction (Marchalot et al. 2014; Sollier et al. 2010), size-controlled nanoparticles synthesization (Kim et al. 2012), and fluid mixing (Shih and Chung 2007; Lee and Kwon 2009; Lee et al. 2010). The realization of all these microcavity-featured microfluidic devices applications relies on the fine and precise control of the microvortices. Currently, considerable efforts toward the development of microcavity-featured microfluidic devices using inertial forces can be observed (Karimi et al. 2013; Sajeesh and Sen 2014; Amini et al. 2014; Zhang et al. 2016). However, only a few studies focus on the effects of microcavity geometry factors on the characteristic of the microvortices (Fishler et al. 2013; Yu et al. 2005; Shen et al. 2015; Oysterman et al. 2016).

Cavity inherently is a flow separation triggering element due to its sharp corners (Yu et al. 2005). Consequently, it is considered as an energy loss component in internal flow systems, which depends on the cavity shape and dimensions. Flow inside rectangular cavities has always been an interesting fluid dynamics question due to mixing, heat transfer and fluid–structure interactions (Haddadi and Di Carlo 2017; Shankar and Deshpande 2000). Historically, cavity flows have been characterized in two or three dimensions, finding different vortex structures in various cavity geometries (Shen and Floryan 1985; Kim et al. 2000; Romero-Mendez et al. 1999; Shankar 1997; Shankar and Deshpande 2000; Heaton 2008). However, most of the research work related to cavities has been on a macroscale. Previously, vortices on microscales are less well known, mainly since flow in microchannels at low Reynolds numbers has been regarded to lack appreciable fluid inertia. Microcavity flows have gained renewed attention only in recent few years since the numerous applications of microvortices in microfluidic devices. Microvortices can be generated when a microchannel is suddenly expanded in width leading to jetting of the main flow stream, the detachment of the boundary layer, and recirculation in the expansion region. It is generally accepted that the vortex formation and evolution rely on the fluid inertia, namely the inlet Reynolds number of the main microchannel flow. When the Reynolds number exceeds a critical value, a microvortex will arise. Increasing the Reynolds number leads to increasing vortex size until the full expansion region is occupied. It is important to note that as the microcavity flow is driven by the shear stress of the main microchannel flow at the entrance area of the microcavity, both the flow profile of the main microchannel flow and geometry of the entrance have a significant influence on the energy transfer from the main microchannel flow to the microvortices.

Lim et al. (2003) first reported the dynamic formation of a microvortex in a small diamond-shaped microcavity (maximal size of 55 μm), which can be used to generate a radial acceleration as high as 10^7m s^{-2} (Shelby et al. 2003) and rotate particles and cells (Shelby et al. 2004). Yu et al. (2005) investigated flow patterns in square microcavities with quite small dimensions (width and length varying between 20×20 and 70×70 μm^2 and the height is 1.5 μm) and determined the critical conditions for the transition from attached flow to separated flow by constructing a flow regime map. They also found that whether the microcavity flow is attached or separated, the microcavities reduce the local resistance to the main microchannel flow. However, this setup is too small for aforementioned microfluidic applications. Using microparticle image velocimetry (micro-PIV) and computational fluid dynamics (CFD) simulations, Fishler et al. (2013) investigated the effects of microcavity geometry and Reynolds numbers ($Re = 0.1$, 1 and 10) on flow phenomena in cylindrical microcavities, finding two flow patterns, namely attached flow and separated flow, the latter featuring single vortex or complex multivortex systems. They also characterized quantitatively the evolution of microvortices (i.e., number, location, center, and the existence of saddle point). In our previous study (Shen et al. 2015), we used the micro-PIV and studied quantitatively the influences of the microcavity aspect ratio (λ = width/length = 0.25–3) and Reynolds numbers (Re = 0–100) on the flow characteristics of rectangular microcavities, finding three different flow patterns: attached flow, transitional flow and separated flow. Oysterman et al. (2016) investigated, experimentally and by modeling, the flow in a long microcavity, finding that the properties of microvortices also depend decisively on the length/width ratio of the rectangular microcavities and the number of microvortices increases from 2 to 4 with the length/width ratio increasing. Recently, there has been considerable interest in understanding particle and cell behaviors in microvortices (Hur et al. 2011; Mach et al. 2011; Park et al. 2009; Zhou et al. 2013). For example, Zhou et al. (2013) simulated the microvortices structure in three dimensions in a 300 × 300 μm^2 microcavity to reveal the reason for the phenomenon that two stable orbits of trapped particles this microcavity observed in experiments of Hur et al. (2011). Moreover, Haddadi and Di Carlo (2017) studied the inertial flow of a dilute suspension of particles over confined rectangular microcavities and discussed the interaction of particles with the vortex inside the microcavities. The flow field structures in microcavities with different sizes (λ = 2, 3 and 5) were illustrated by fluorescent images, finding that the mechanics of particle dynamics in microvortices is very complex. Despite the great progress of revealing the microcavity flow behaviors in the present research studies, the effects of geometry factors, for example the microcavities actual size and the hydraulic diameter (D_H) of the main microchannel, on the evolution of microvortices have not been investigated systematically, which are still actual fundamental issues for microcavity-featured microfluidic devices design and applications.

In this study, using the micro-PIV and CFD simulations, we investigate quantitatively the evolution of microvortices in square microcavities (λ = 1) with four different sizes ($W_C = L_C$ = 100, 200, 400, 800 μm) at wider range of Reynolds numbers (Re = 0–400) than that in our previous study (Shen et al. 2015). We focus on the influences of microcavity actual sizes and the hydraulic diameter of the main microchannel (D_H = 100, 133 μm) on the evolution of microvortices. The characteristics of the microvortices are investigated quantitatively in detail. Moreover, the critical Reynolds numbers for the emergence of microvortices and the transformation of different flow patterns are determined. The results will deepen the understanding of the microvortex behaviors in microcavities and provide a useful guideline for the design of microcavity-featured microfluidic devices and their applications.

2 Methods

2.1 Microfluidic device

To characterize the effect of actual size of the microcavities and the hydraulic diameter (D_H) of the main microchannel on the evolution of microvortices systematically, we designed two microfluidic chips consisting of four different square microcavities located on one side of a straight main microchannel for each chip, as shown in Fig. 1a. Figure 1b shows a microvortex generated within a square microcavity. The confined microcavity flow is driven by the main

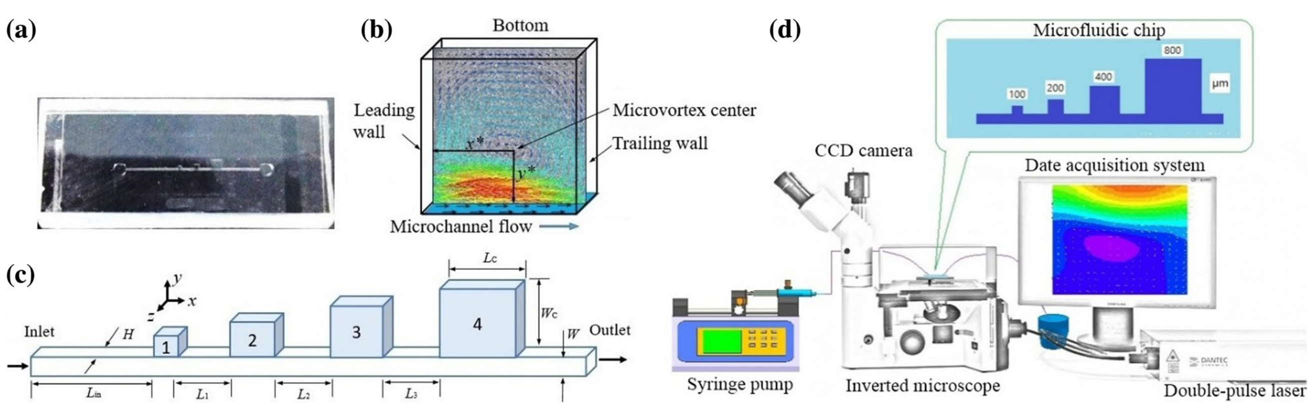

Fig. 1 **a** Snapshot of one PDMS microfluidic chip (40 × 20 mm^2) consisting of four different square microcavities located on one side of a straight microchannel. **b** A microvortex in a square microcavity driven by the main microchannel flow. **c** A schematic illustration of the microfluidic chips. **d** A schematic illustration of the experimental setup. The width and length of the four microcavities are $W_C = L_C$ = 100, 200, 400, and 800 μm, respectively. The distances between them are 1 mm. The distance from the inlet to the first microcavity is L_{in} = 3 mm. Both the microchannel and microcavities share the same depth H = 100 μm. The microchannel width W = 100 and 200 μm

microchannel flow at the microcavity entrance area. The normalized dimensionless coordinates for the microcavities are defined as $x^* = x/L_C$ and $y^* = y/W_C$. The geometry of an open microcavity is similar to a backward facing step followed by a forward facing step with a primary microvortex confined by the microcavity walls. The microcavities are similar to rectangular microcavities used in previous studies (Hur et al. 2011; Mach et al. 2011; Park et al. 2009; Yew et al. 2013; Yu et al. 2005; Zhou et al. 2013). Figure 1c schematically illustrates the geometric parameters of the microfluidic chips. The width and length of the four microcavities are $W_C = L_C = 100$, 200, 400, and 800 µm, respectively. The microchannel width has two values $W = 100$ and 200 µm. The microchannel and microcavities have the same depth ($H = 100$ µm). The hydraulic diameters of the main microchannel, defined as $D_H = 2WH/(W+H)$, are 100 and 133 µm according to the microchannel widths. To insure fully developed inlet flow conditions, the distance from the inlet to the first microcavity is fixed at $L_{in} = 3$ mm, which is the same as the maximum entrance length $L_e \sim 0.6D_H/(1+0.035Re)+0.056ReD_H$ at $D_H = 133$ µm for $Re = 400$, according to the empirical correlation for low-Reynolds-number channel flow (Shah and London 1978). The spaces between two adjacent microcavities are fixed at $L_1 = L_2 = L_3 = 1000$ µm, which is 7.5 times larger than the maximal hydraulic diameters. Note, as the velocity profiles at the leading wall of each microcavity are still parabolic (see Supplementary Figure), the interaction effect of the neighboring microcavities was not considered in this study. The total length of the main microchannel is 12.5 mm. The microfluidic chips were made of polydimethylsiloxane (PDMS) by standard soft lithography techniques (Duffy et al. 1998). The surface roughness of the microchannel is below 0.5 µm.

As the microcavity flow is driven by the main microchannel flow, the microcavity flow is controlled by two parameters, namely the flow characteristics of the main microchannel and the geometry factors of the microcavities (Yew et al. 2013; Yu et al. 2005). The main microchannel flow can be characterized by the inlet Reynolds number, which can be calculated as $Re = \rho UD_H/\mu$, where ρ and μ are the fluid density and viscosity. The velocity scale U is taken as the average velocity in the main microchannel given by $U = Q/\rho WH$, where Q is volumetric flow rate. Moreover, the effect of the hydraulic diameter (D_H) of the main microchannel on the microcavity flow behaviors should be considered. The microcavity geometry can be characterized by the dimensionless width ($\varepsilon = W_C/H$) and length ($\delta = L_C/H$) and the microcavity aspect ratio ($\lambda = W_C/L_C$) (Shen et al. 2015). However, the problem that how the absolute microcavity dimensions affect the microcavities flow phenomena is still not clear, which will be focused in this study by keeping the microcavities aspect ratio (λ) at 1.

2.2 Experimental setup

In the experiments, deionized water ($\rho = 10^3$ kg/m^3 and $\mu = 10^{-3}$ Pa s) at 20 °C was used as the test fluid and seeded with polystyrene red fluorescent beads (mean diameter of 0.86 µm, the density of 1.05 g/mm^3, Duke Scientific) to visualize the microcavity flow. Tween 20 (0.2% v/v) was added in the test fluid as a surfactant to reduce the chance of the seeding particles adhesion to the walls of the microcavities. Before experiments, the seeded test fluid was placed in an incubator 30 °C for 4 h. Then, to improve the experimental accuracy, only the suspension of buoyant particles was selected and diluted for the experiments. To prevent trapping of bubbles in the microcavities, the microchannel was flushed with Tween 20 (1% v/v) solution before injecting the actual test fluid.

The size of the seeding particles should be relatively small to reduce the velocity lag of a particle (Raffel et al. 2007). However, the seeding particles must be large enough to be adequately imaged and to dampen the effects of Brownian motion (Wereley and Meinhart 2010). Therefore, particles with a mean diameter of 0.86 µm were selected as the seeding particles in our experiments. The ratio of seeding particles size to the minimum feature size of the microcavities (100 µm) is 1:116, which is low and ensures that the particle responds to a local point force rather than to a global integration of momentum exerted by the fluid flow. The seeding particles are considered to have good following property, and the influence of the particles on the fluid could be ignored.

A schematic diagram of the experimental setup is shown in Fig. 1d, which includes the homemade microfluidic chips, a syringe pump (Harvard Apparatus, PHD2000), and a micro-PIV system (Dantec Dynamics), which is a nonintrusive technique applied to evaluate the characteristics of the flow field (Lindken et al. 2009; Wereley and Meinhart 2010; Williams et al. 2010). The volumetric flow rate (Q) ranges from 0.8 to 3.6 ml/min corresponding to $Re = 89$–400. To ensure the accuracy of the measurements, it is necessary to stabilize the stream before initiating measurements. The micro-PIV system consists of a double-pulse Nd: YAG laser, a high-speed high-resolution double-frame CCD camera, an inverted microscope (Leica), a signal synchronizer, and a 3D mobile stage. The details of the micro-PIV system were introduced in our previous studies (Shen et al. 2015). Briefly, the particle images were first captured with a resolution of 1344×1024 pixels, at a rate of 6 frames per second (fps) with the exposure time of $10 \sim 200$ µs according to the flow rate, and then recorded on a computer for results analyses using a software (Dantec Dynamics V3.40). The acquired particle images were analyzed with an adaptive cross-correlation (ACC) algorithm. The interrogation area was 32×32 pixel (50% overlap). Moreover, the least squares

Gauss fitting algorithm was used to detect the peak on the correlation plane to reduce measurement uncertainty and to improve the signal-to-noise ratio. Particle images at the mid-depth *x*–*y* plane of the microcavities ($z = 50$ μm) were recorded by adjusting the position of an objective (10×, numerical aperture 0.4) through the 3D mobile stage. The thickness of the measurement plane is about 13.8 μm according to the report of Wereley and Meinhart 2010. The micro-PIV results are depth-averaged over the effective depth of correlation and to be compared with CFD simulations.

2.3 Numerical models

Using a commercial CFD software ANSYS (Fluent, 16.0), the microchannel and microcavities were modeled in three dimensions according to their actual dimensions. The model was created and meshed using structured hexahedral volume meshes. Mesh refinement and independence were tested. Simulations were performed with 87,608 cells. The numerical model was simplified by assuming a steady state flow regime. The governing equations are the continuity equation and incompressible Navier–Stokes equations. A finite volume method was utilized to turn the governing partial differential equations into a system of algebraic equations, which are numerically integrated over each of the computational cells using a collocated cell-centered variable arrangement. A second-order upwind scheme was used for the momentum equations, and the SIMPLEC scheme is used for pressure calculations.

The physical properties of water were applied to the fluid in the simulation (dynamic viscosity $\mu = 10^{-3}$ Pa s, density $\rho = 10^3$ kg/m^3). At the microchannel walls, a nonslip boundary condition was applied. For the inlet volume flow rates corresponding to $89 < Re < 400$ were set, while the outlet was set to a fixed-pressure boundary condition. To achieve convergence, the residuals of continuity and momentum equations are required to be below 10^{-5}. Combinations of *x*-, *y*- and *z*-cut were processed to obtain velocity profiles and to trace the microvortices. The simulation results were compared with the experiments, finding a good agreement.

3 Results and discussion

3.1 Effect of Reynolds number (*Re*)

In the experiments, flow in the main microchannel is laminar ($Re < 400$) and the velocity profile is nearly parabola. To reveal the influence of the inlet Reynolds number on the flow patterns in the microcavities, flow in a 400×400 μm^2 microcavity was measured thoroughly in the micro-PIV experiments with *Re* varying from 89 to 400, as shown in Figs. 2 and 3. The hydraulic diameter of the main microchannel is $D_H = 133$ μm. Figure 2 shows a series of 2D velocity vector fields at the mid-depth planar of the microcavity, and

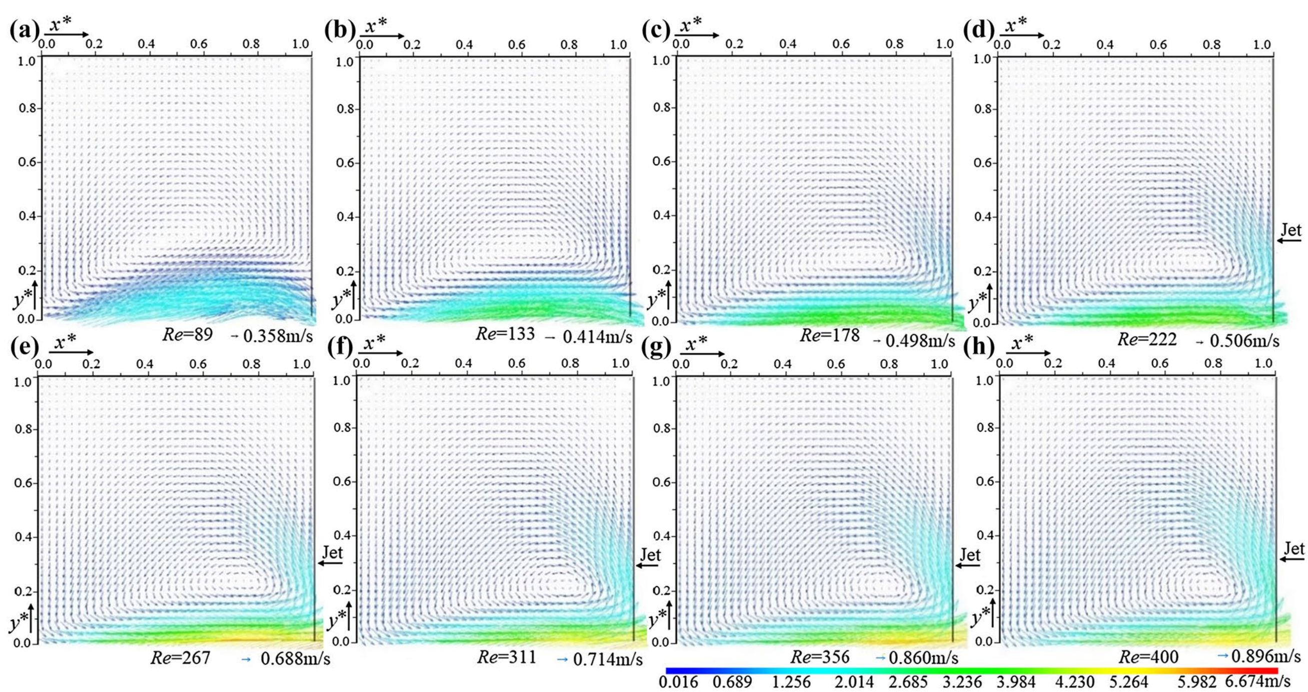

Fig. 2 Micro-PIV measurements of velocity vector fields in the 400×400 μm^2 microcavity at different Reynolds numbers with $D_H = 133$. **a** $Re = 89$, **b** $Re = 133$, **c** $Re = 178$, **d** $Re = 222$, **e** $Re = 267$, **f** $Re = 311$, **g** $Re = 356$, **h** $Re = 400$

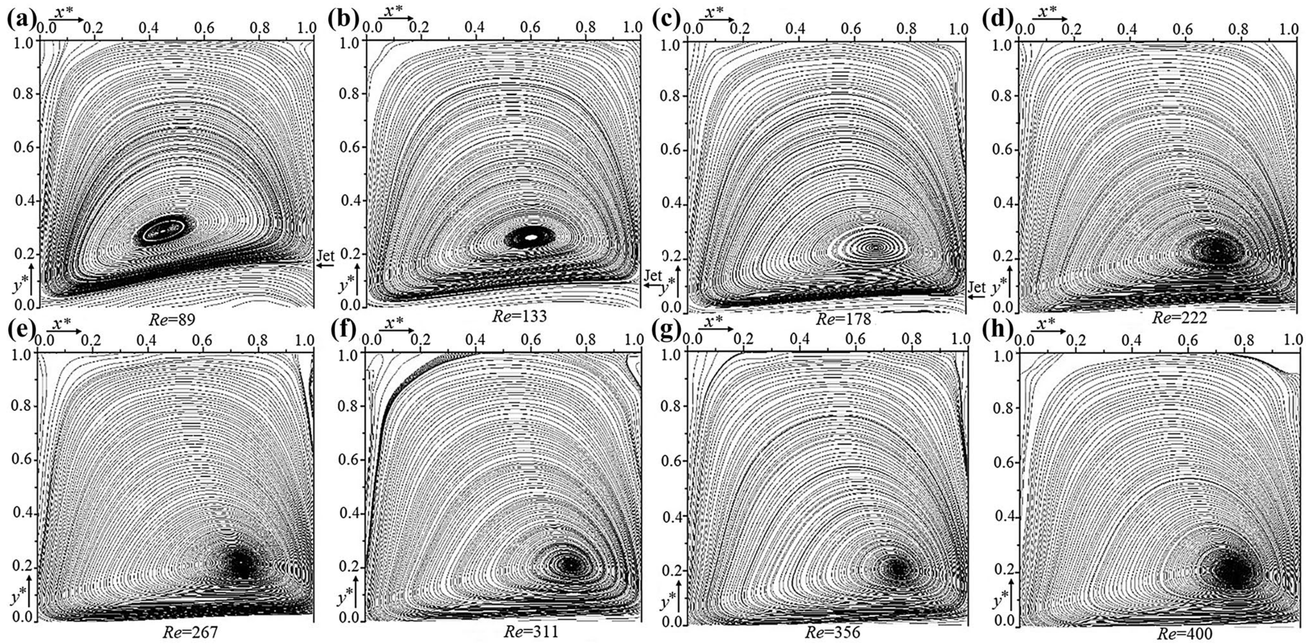

Fig. 3 The corresponding streamline plots in the 400 × 400 μm^2 microcavity at various Reynolds numbers with $D_H = 133$. **a** $Re = 89$, **b** $Re = 133$, **c** $Re = 178$, **d** $Re = 222$, **e** $Re = 267$, **f** $Re = 311$, **g** $Re = 356$, **h** $Re = 400$. The arrow shows the stagnation point on the trailing wall

Fig. 3 shows the corresponding streamline plots. Note that as the velocity of the main microchannel flow is about one or two orders of magnitude higher than the microvortices, it is impossible to measure simultaneously the flow across the entire geometry (i.e., the main microchannel and microcavity) using the same acquisition frame rate in the experiments. Only the velocity vectors fields of the microcavity were measured. Each velocity vector also indicates the velocity magnitude by its length. Note, the microcavities dimensions were normalized by $x^* = x/L_C$ and $y^* = y/W_C$.

The results indicate that there is always only one microvortex generated in the microcavity at $Re > 89$. The main microchannel flow separates and forms a jet effect near the entrance of the microcavity. According to the definition of flow patterns in our previous study (Shen et al. 2015), all the microcavity flows at $Re > 89$ are separated flow, which meaning that the microvortex is strong enough and pushes the main flow streamlines out of the microcavity. In this study, the Re values are much higher than that in our previous report ($Re < 100$) (Shen et al. 2015). Only the separated flow is more suitable for particles/cells isolation (Mach et al. 2011; Zhou et al. 2013; Khojah et al. 2017). When $Re > 178$, the microvortex occupies the whole microcavity, and once particles or cells entry the microvortex, they will be trapped and orbit within the microvortex (Hur et al. 2011; Sollier et al. 2014). Moreover, the streamline plots in Fig. 3a–c indicate that the vertical streamlines and the main flow streamlines separate in the area near a stagnation point on the trailing wall. Particles or cells may collide with the trailing wall near the stagnation point and be trapped in the microcavity. This collide-triggered trapping mechanism was studied in our previous report (Shen et al. 2017a, b). With the Re increasing from 89 to 178, the stagnation point moves down toward the main microchannel. From the results, we can speculate that the microcavity flows at $89 < Re < 178$ are more suitable for particles trapping, while particles will flow over the microcavity mouth before entering the microcavity at $Re > 178$. Besides, the velocity vector fields in Fig. 2 show there is a jet flow in the area near the trailing wall, where the flow velocity vectors change significantly. The jet phenomenon becomes more obvious with Re increasing, as shown in Fig. 2d–h. The jet flow with high velocity will have a significant influence on the orbiting trajectory of trapped particles/cells. Furthermore, with Re increasing from 89 to 400, the microvortex structure changes. As the microvortex is driven by the main microchannel flow, the shear stress (τ) between them increases with Re increasing, which induces that both the size and average velocity magnitude of the microvortex increase.

3.2 Effect of the hydraulic diameter (D_H)

Previous researchers studied the influence of Reynolds number only by changing the inlet flow rate (Fishler et al. 2013). The effect of the hydraulic diameter (D_H) of the main microchannel on the microcavity flow behaviors has not been reported as we know. In this experiment, the hydraulic diameter was changed to $D_H = 100$ μm by using the second microfluidic chip with the main microchannel width $W = 100$ μm. In order to avoid the damage of microfluidic chip induced by the high pressure of the inlet fluid, the inlet flow rate was set from 0.4 to 1.8 ml/min, corresponding *Re* varying from 67 to 300.

Figure 4 shows the velocity vector fields in the same 400×400 μm^2 microcavity with Reynolds numbers varying from 67 to 300, while Fig. 5 shows the corresponding streamline plots of the microvortices. By comparing Figs. 4c and 5c with Figs. 2b and 3b, it is found that

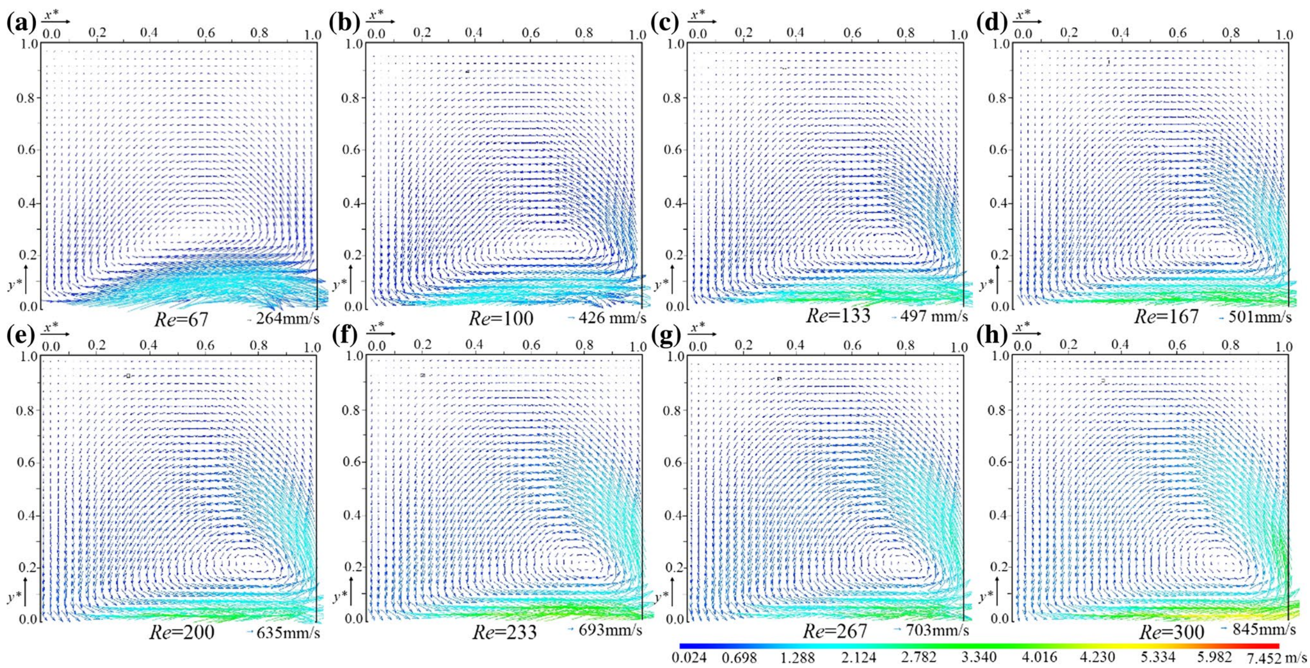

Fig. 4 Micro-PIV measurements of velocity vector fields in the 400×400 μm^2 microcavity at different Reynolds numbers with $D_H = 100$. **a** *Re* = 67, **b** *Re* = 100, **c** *Re* = 133, **d** *Re* = 167, **e** *Re* = 200, **f** *Re* = 233, **g** *Re* = 267, **h** *Re* = 300

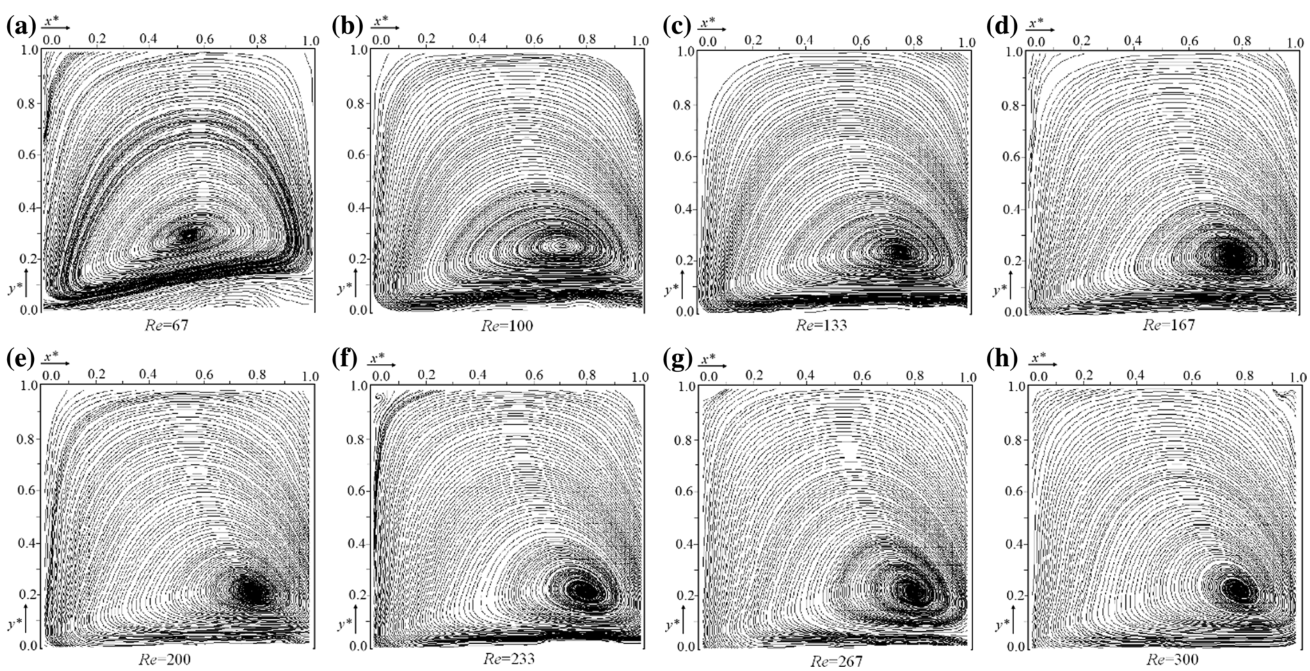

Fig. 5 The corresponding streamline plots in the 400×400 μm^2 microcavity at various Reynolds numbers $D_H = 100$. **a** *Re* = 67, **b** *Re* = 100, **c** *Re* = 133, **d** *Re* = 167, **e** *Re* = 200, **f** *Re* = 233, **g** *Re* = 267, **h** *Re* = 300

although the Reynolds numbers for these two cases are the same ($Re = 133$), the microvortex size with $D_H = 100$ μm is bigger than that with $D_H = 133$ μm. The microvortex center in Fig. 5c is closer to the trailing wall than that in Fig. 3b. In Fig. 5c with $D_H = 100$ μm, the microvortex occupies the whole microcavity and its average velocity magnitude increases. The results indicate that the flow shear effect of the main microchannel flow on the microcavity flow with $D_H = 100$ μm is more significant than that with $D_H = 133$ μm. One reason is that the average velocity in the main microchannel with $D_H = 100$ μm is 1.33 times higher than that with $D_H = 133$ μm. Considering the difference in the microchannel width, the flow shear stress (τ) is about 2.66 times higher in the microchannel with $D_H = 100$ μm calculated using simplified theoretical model. The other reason is that flow in the main microchannel with high aspect ratio (H/W) has a stronger effect on the microcavity flow and is more suitable for microvortex formation at the same Reynolds numbers. The micro-PIV results indicate that the hydraulic diameter (D_H) has significant influences on the microcavity flow.

Besides, in Figs. 4c and 2c the average flow velocities are the same value ($U = 1.33$ m/s), while the Reynolds numbers are 133 and 178, respectively. The microvortex size in Fig. 4c with $D_H = 100$ μm is bigger than that with $D_H = 133$ μm in Fig. 2c, which also verifies the above-mentioned second reason. Moreover, although the Reynolds numbers are the same ($Re = 267$), the microvortex size in Fig. 4g with $D_H = 100$ μm is also bigger than that with $D_H = 133$ μm in Fig. 2e. The results indicate that the effect of the main flow on the microcavity flow behaviors cannot be characterized by the inlet Reynolds number independently, and the geometry factors of the main microchannel, including the hydraulic diameter (D_H) and the aspect ratio of the microchannel across section, also have significant effects on the microcavity flow.

To thoroughly understand the influences of the hydraulic diameters (D_H) and inlet Re on evolution of microvortices, we investigated the precise location (x^* and y^*) of the microvortex center at Re varying from 89 to 400, as shown in Fig. 6. The results show that Re has a significant influence on the location of the microvortex center. With Re increasing, the x^* value increases, meaning that the microvortex moves toward the trailing wall. As the confinement of the trailing wall, the vortical flow between the microvortex center and the trailing wall will become a jet flow, which velocity increases with Re increasing. For the microfluidic chip with $D_H = 133$ μm, the x^* value keep at about 0.75 finally whatever the Re keeps on increasing. On the contrary, the y^* value decreases from 0.28 to 0.20 as Re increases. The flow between the microvortex center and the main microchannel flow also becomes stronger with Re increasing as the shear stress effect becomes stronger. For the microfluidic

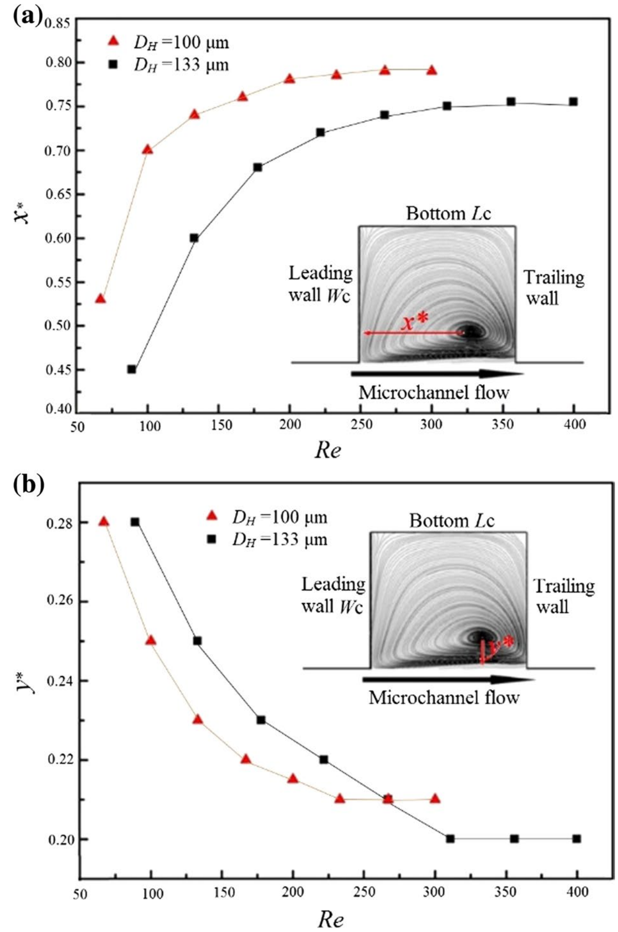

Fig. 6 Effects of the hydraulic diameters (D_H) on **a** x^* and **b** y^* locations of the microvortex center in the 400×400 μm^2 microcavity as a function of Re

chip with $D_H = 100$ μm, the x^* value increases more quickly and keeps at about 0.79 after Re reaches at 267, which also indicates that the shear stress effect in the microchannel with $D_H = 100$ μm is more significant than that with $D_H = 133$ μm at the same flow conditions. Moreover, with Re increasing the y^* value decreases from 0.28 to 0.21 at $Re = 300$, which is a little higher than y^* of 0.20 with $D_H = 133$. We speculate that the reason is that the main microchannel flow pushes the microvortices toward the y-direction as the wall confinement effect on the main microchannel flow with $D_H = 100$ μm ($W = 100$ μm) is more significant.

3.3 Effect of microcavities size

The effects of actual size of the microcavities on the microcavity flow characteristics, which have practical significance in microfluidic device design, have not been addressed in previous studies (Hur et al. 2011; Mach et al. 2011; Park et al. 2009; Yew et al. 2013; Yu et al. 2005; Zhou et al. 2013). Here, we measured and simulated the velocity vector fields in square microcavities with four different sizes, namely $W_C = L_C = 100$, 200, 400, and 800 μm, as shown in Figs. 7 and 8. Note, the microcavities sizes were normalized by $x^* = x/L_C$ and $y^* = y/W_C$.

Figure 7 shows that at $Re = 30$, the flow is separated in the microcavity with sizes of 100×100 μm^2 and a microvortex occurs in it (Fig. 7a, b), while in the 400×400 μm^2 microcavity (Fig. 7c) and the 800×800 μm^2 microcavity (Fig. 7d) are transitional flow and attached flow, respectively. It is found that although the flow conditions are maintained same ($Re = 30$) and the aspect ratios of the microcavities are all $\lambda = 1$, the flow patterns in the microcavities with different sizes change obviously. It indicates that with the microcavity size increasing, the shear stress effect of the main microchannel flow decreases. The critical Reynolds number (Re_c) of microvortices generation in smaller size microcavities is lower than that in bigger microcavities. The occurrence of separated flow pattern in a microcavity depends not only on high enough Reynolds numbers but also on the geometry factors of the microcavity, namely the aspect ratio and actual size. Figure 8 shows that the flow patterns in the four microcavities are all separated at $Re = 107$. However, the microvortex morphology changes obviously.

To show the microvortex morphology clearly, the simulated streamline plots of microvortices in microcavities with different sizes for $D_H = 100$ at $Re = 200$ are shown in Fig. 9. It is found that the microvortex morphology evolves gradually from round shape in the 100×100 μm^2 microcavity (Fig. 9a) to half-moon shape in the 800×800 μm^2 microcavity (Fig. 9d), although other influence factors are the same. With the microcavities size increasing, the microvortex center moves toward the trailing wall of the microcavities and the normalized distance between the microvortex center and the microcavity mouth decreases, as shown in Fig. 9. Please note that although the evolution of microvortices morphology is the similar to that in Figs. 3, 5, and 6, where the microcavity size is fixed at $W_C = L_C = 400$ μm and the evolution of microvortices is determined by Re, the

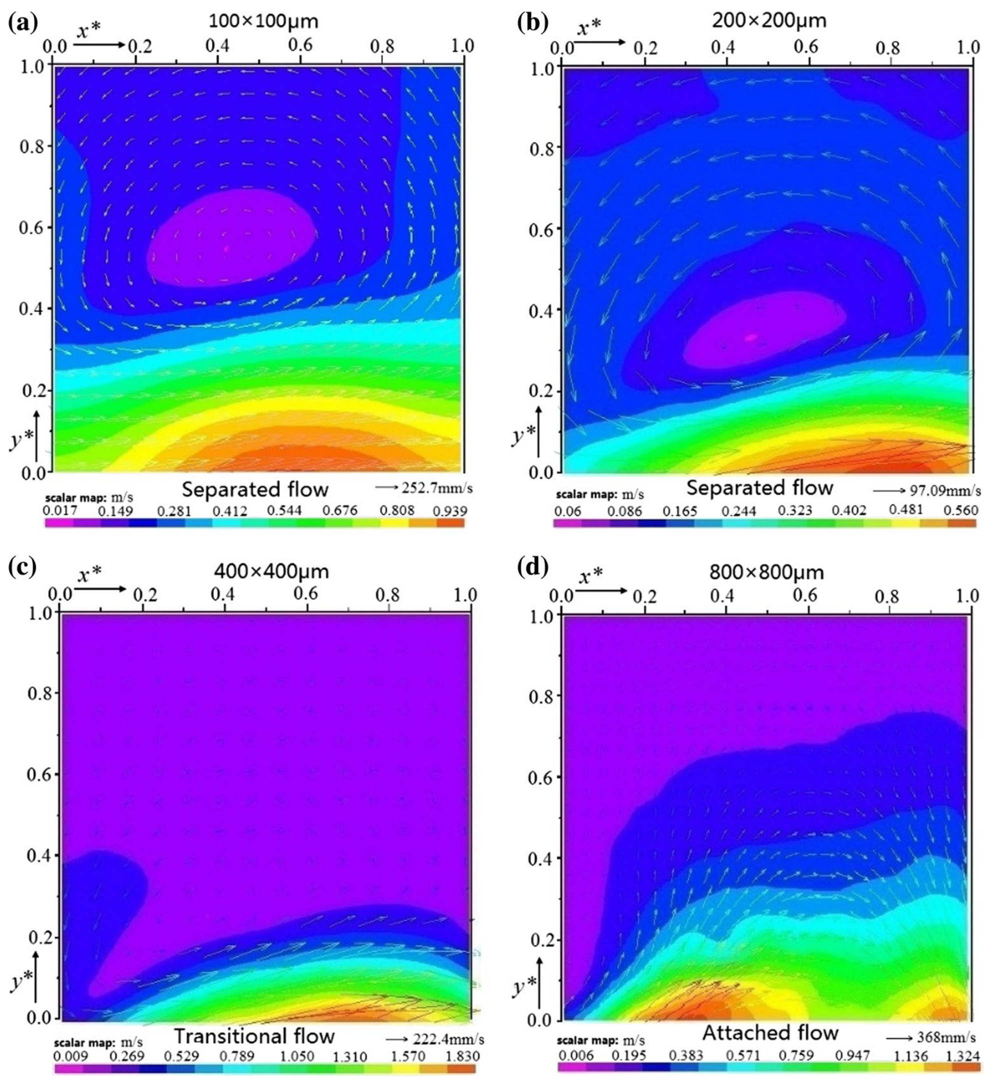

Fig. 7 Micro-PIV results of flow patterns in microcavities with different sizes for $D_H = 100$ at $Re = 30$. **a** 100×100 μm^2, **b** 200×200 μm^2, **c** 400×400 μm^2, **d** 800×800 μm^2

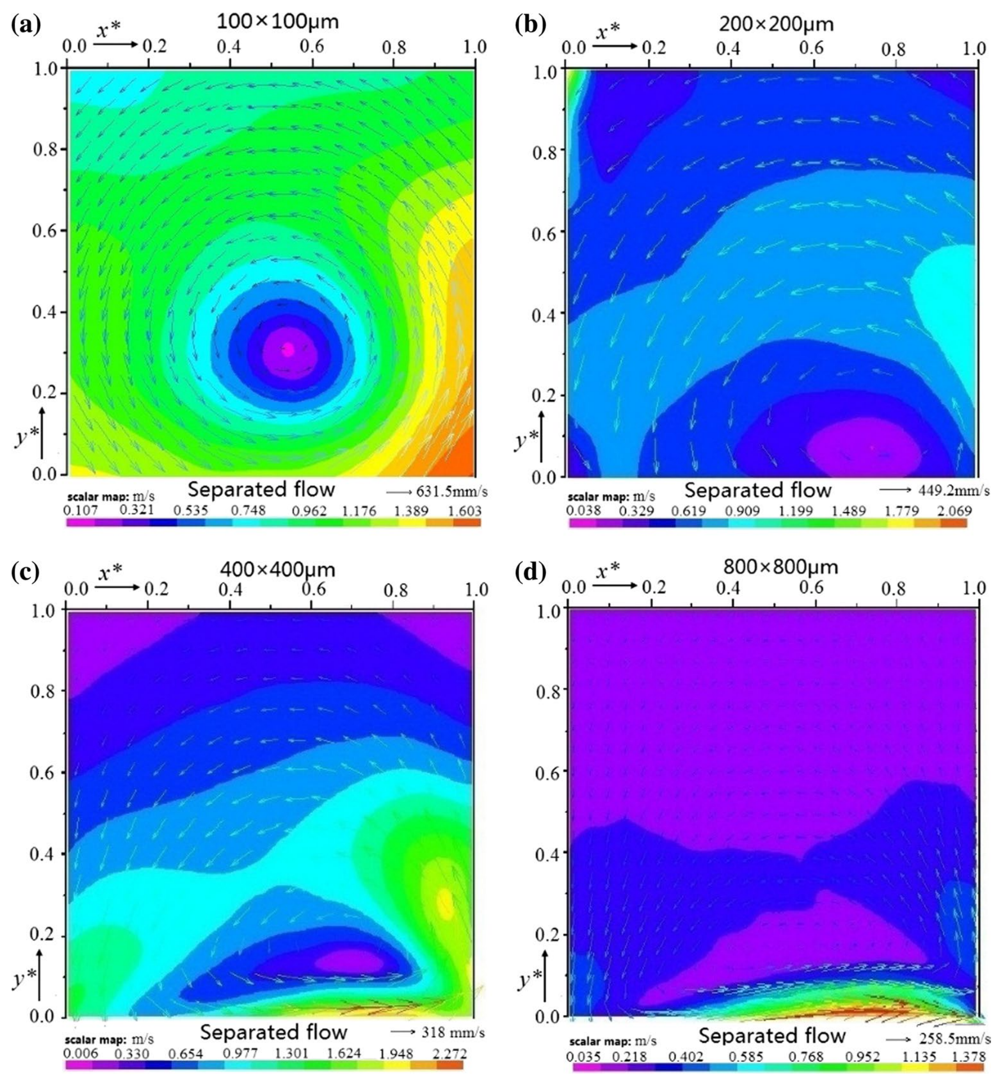

Fig. 8 Micro-PIV results of flow patterns in microcavities with different sizes for $D_H = 100$ at $Re = 107$. **a** 100 × 100 μm^2, **b** 200 × 200 μm^2, **c** 400 × 400 μm^2, **d** 800 × 800 μm^2

mechanisms of microvortices evolution are different distinctly. In Fig. 9, the microvortices morphology depends on the combined effects of the shear stress of the main microchannel flow at the entrance of the microcavities and the confinement of the microcavities walls.

In order to investigate the detailed flow characteristics quantitatively inside the microcavities, the corresponding horizontal velocity profiles (u_x) were extracted from the results of the Figs. 7 and 8, as shown in Fig. 10a, b. Note that the horizontal velocity profiles (u_x) were plotted along the centerline in the *y*-direction. It is found that the velocity profiles in different microcavities vary significantly and the u_x value decays rapidly with y^* increasing. In Fig. 10a, microvortices occur in microcavities with $W_C = L_C = 100$, 200, and 400 μm at *Re* of 30; the u_x values fall below the zero-line at red X-points (as shown in the figure), which indicates the y^* locations of the microvortex center. Figure 10b shows the similar results at $Re = 107$ that microvortices occur in the microcavities inducing the u_x value falls from positive to negative. The red X-points indicate the locations of the microvortex center. Moreover, the velocity of the microvortices is about two orders of magnitude slower than the main microchannel flow. The results of the u_x velocity profiles for the three flow patterns are accordant with our previous results (Shen et al. 2015). Moreover, in Fig. 10b, the microvortices velocity at $y^* > 0.6$ increases with the microcavities size decreasing from 800 × 800 μm^2 to 100 × 100 μm^2, which means the small size microcavities may have better heat and mass transfer performance.

The corresponding shear stress distributions (τ) plotted along a line at the bottom of the microcavities were also extracted from results of Fig. 9, showing that the τ values

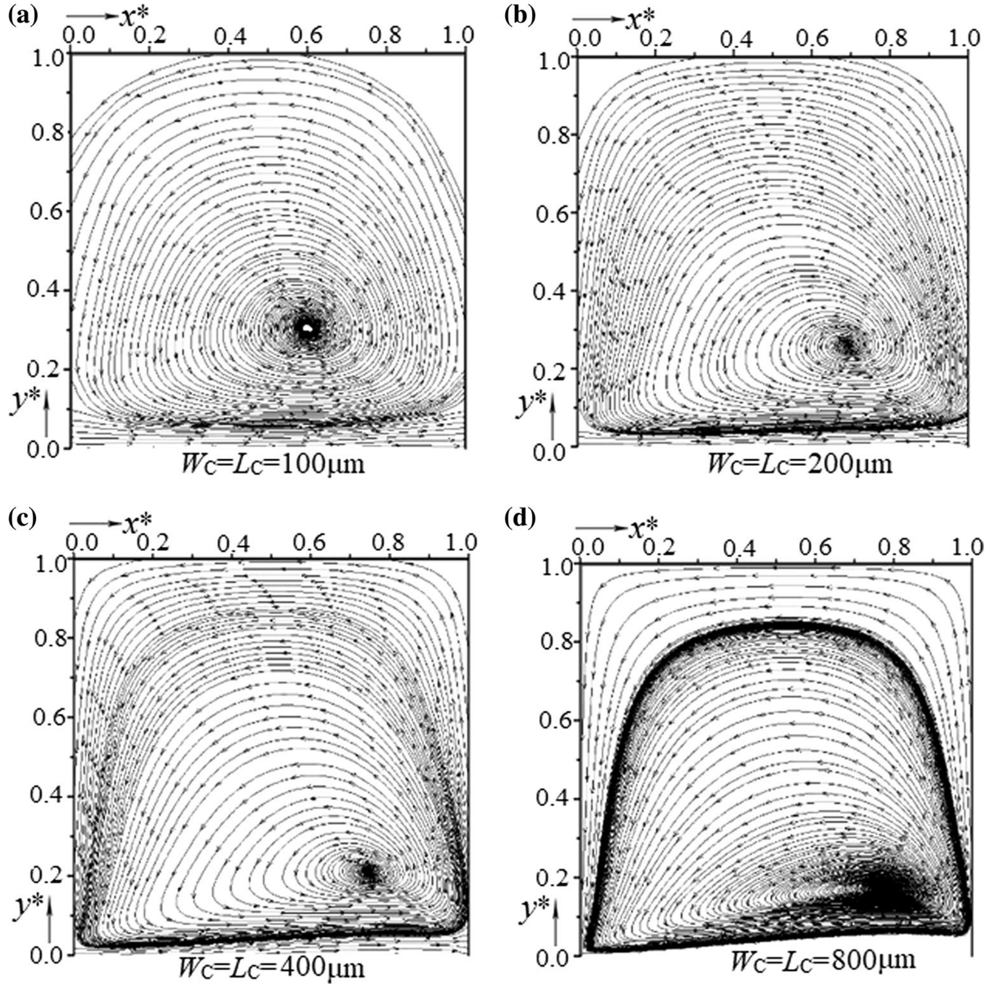

Fig. 9 The simulated streamline plots of microvortices in microcavities with different sizes for $D_H = 100$ at $Re = 200$. **a** $100 \times 100\ \mu m^2$, **b** $200 \times 200\ \mu m^2$, **c** $400 \times 400\ \mu m^2$, **d** $800 \times 800\ \mu m^2$

decrease with the microcavity size increasing (Fig. 10c). The reason is that the shear stress effect of the main microchannel flow on the microvortex is more significant in smaller microcavity than that in the bigger microcavity. The τ values in the $800 \times 800\ \mu m^2$ microcavity are very small and near to zero, which means that microcavities with bigger size are more suitable for cell culture. The maximum τ values in the $100 \times 100\ \mu m^2$ and $200 \times 200\ \mu m^2$ microcavities are 0.75 and 4.75 Pa.

3.4 Flow regimes

To establish a useful microfluidic design guideline, we mapped the critical Reynolds number (Re_c) for the transition of different flow patterns at each microcavity as a function of the microcavity size and Re, as shown in Fig. 11. This phase diagram shows that the microcavity size and the Re_c have a linear relationship nearly for the flow patterns transition. With the microcavity size increasing, the Rec increases. In $100 \times 100\ \mu m^2$ microcavity, the flow is separated even at very low Reynolds number ($Re_c = 12$). In $800 \times 800\ \mu m^2$ microcavity, the Re_c values for the transitional flow and separated flow are 30 and 107 for experimental results, respectively. The simulation is in good agreement with the experimental results.

4 Conclusions

Using both micro-PIV experiments and numerical simulations, we quantitatively studied the effect of the geometry factors, namely the main microchannel width (W) and the microcavity actual size ($L_C = W_C$), and inlet Reynolds numbers on the flow characteristics in square microcavities located on one side of a main straight microchannel. The flow field structures in microcavities with different sizes ($L_C = W_C = 100$, 200, 400, and 800 μm) were obtained at wider Reynolds numbers ($Re = 0$–400) with the main microchannel hydraulic diameter $D_H = 100$ and 133 μm. The results show that the flow behaviors and microvortices morphology, determined by the interaction of the shear stress effect and microcavity walls confined effect, are different in

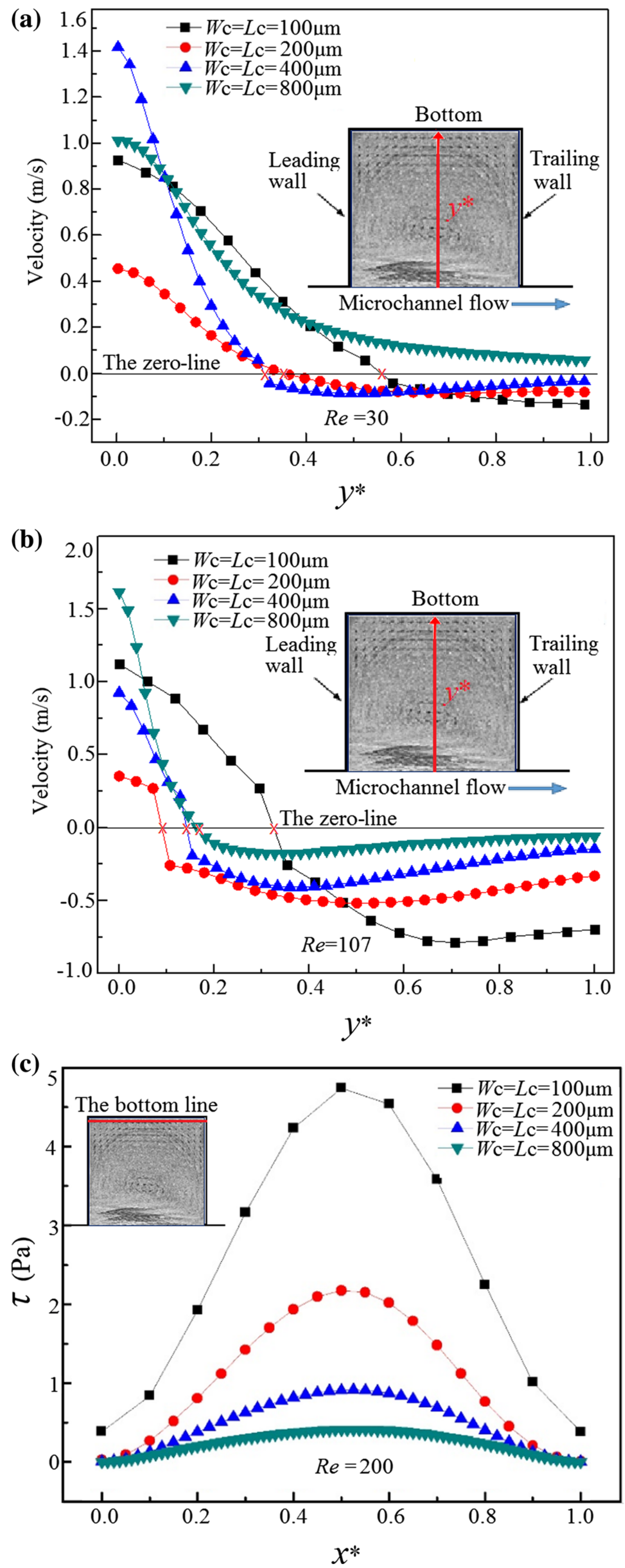

Fig. 10 **a** Corresponding horizontal velocity profiles (u_x) plotted along the centerline in the y-direction at $Re=30$ and **b** at $Re=107$. **c** Corresponding shear stress distributions (τ) plotted along a line at the bottom of the microcavities at $Re=200$

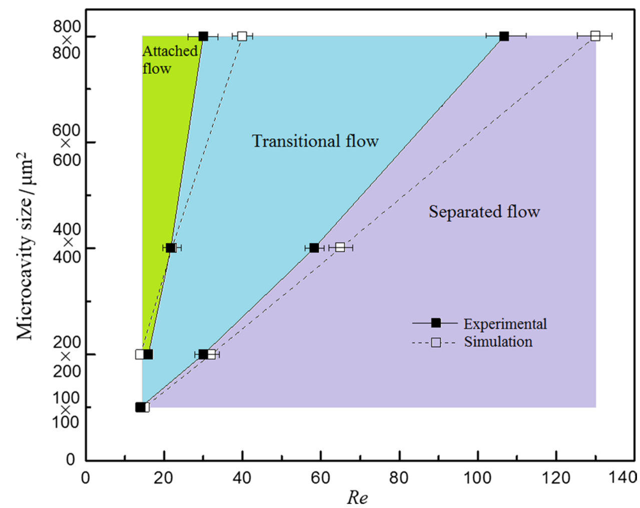

Fig. 11 Flow regime map for different flow patterns based on the microcavity size and Re ($D_H=100$ μm)

different square microcavities at the same Reynolds numbers. Both the main microchannel width and the microcavity actual size have significant influences on the flow characteristics. Moreover, a flow regime map in the microcavities has been constructed, where the critical parameters for the transform of flow patterns are determined. The results will provide a useful guideline for design and applications of microcavity-featured microfluidic devices.

Acknowledgements The authors acknowledge the support of the Beijing Municipal Natural Science Foundation (7152012), General Program of Science and Technology Development Project of Beijing Municipal Education Commission (KM201610005002) and Natural Science Foundation of China (11572013).

References

Amini H, Lee W, Di Carlo D (2014) Inertial microfluidic physics. Lab Chip 14(15):2739–2761

Anna SL (2016) Droplets and bubbles in microfluidic devices. Annu Rev Fluid Mech 48:285–309

Baroud CN, Gallaire F, Dangla R (2010) Dynamics of microfluidic droplets. Lab Chip 10(16):2032–2045

Bremond N, Thiam AR, Bibette J (2008) Decompressing emulsion droplets favors coalescence. Phys Rev Lett 100(2):024501

Chiu D (2007) Cellular manipulations in microvortices. Anal Bioanal Chem 387:17–20

Cioffi M, Moretti M, Manbachi A, Chung BG, Khademhosseini A, Dubini G (2010) A computational and experimental study inside microfluidic systems: the role of shear stress and flow recirculation in cell docking. Biomed Microdevices 12:619–626

Duffy DC, McDonald JC, Schueller OJA, Whitesides GM (1998) Rapid prototyping of microfluidic systems in poly (dimethylsiloxane). Anal Chem 70:4974–4984

Fan LL, He XK, Han Y, Du L, Zhao L, Zhe J (2014) Continuous size-based separation of microparticles in a microchannel with symmetric sharp corner structures. Biomicrofluidics 8(2):024108

Fishler R, Mulligan MK, Sznitman J (2013) Mapping low-Reynolds-number microcavity flows using microfluidic screening devices. Microfluid Nanofluid 15:491–500
Haddadi H, Di Carlo D (2017) Inertial flow of a dilute suspension over cavities in a microchannel. J Fluid Mech 811:436–467
Haller A, Spittler A, Brandhoff L, Zirath H, Puchberger-Enengl D, Keplinger F, Vellekoop MJ (2015) Microfluidic vortex enhancement for on-chip sample preparation. Micromachines 6(2):239–251
Heaton CJ (2008) On the appearance of Moffatt eddies in viscous cavity flow as the aspect ratio varies. Phys Fluids 20:103102–103111
Hsu CH, Di Carlo D, Chen C, Irimia D, Toner M (2008) Microvortex for focusing, guiding and sorting of particles. Lab Chip 8:2128–2134
Huang H, Yu Y, Hu Y, He X, Berk UO, Yarmush ML (2017) Generation and manipulation of hydrogel microcapsules by droplet-based microfluidics for mammalian cell culture. Lab Chip 17:1913–1932
Hur SC, Tse HTK, Di Carlo D (2010) Sheathless inertial cell ordering for extreme throughput flow cytometry. Lab Chip 10: 274–280
Hur SC, Mach AJ, Di Carlo D (2011) High-throughput size-based rare cell enrichment using microscale vortices. Biomicrofluidics 5:022206
Jang YH, Kwon CH, Kim SB, Selimović Š, Sim WY, Bae H, Khademhosseini A (2011) Deep wells integrated with microfluidic valves for stable docking and storage of cells. Biotechnol J. 6(2):156–164
Karimi A, Yazdi S, Ardekani AM (2013) Hydrodynamic mechanisms of cell and particle trapping in microfluidics. Biomicrofluidics 7(2):21501
Khabiry M, Chung BG, Hancock MJ, Soundararajan HC, Du Y, Cropek D, Lee WG, Khademhosseini A (2009) Cell docking in double grooves in a microfluidic channel. Small 5(10):1186–1194
Khojah R, Stoutamore R, Di Carlo D (2017) Size-tunable microvortex capture of rare cells. Lab Chip. https://doi.org/10.1039/c7lc00355b
Kim JH, Oztekin A, Neti S (2000) Instabilities in viscoelastic flow past a square cavity. J Non-Newtonian Fluid Mech 90:261–281
Kim Y, Lee Chung B, Ma M, Mulder WJM, Fayad ZA, Farokhzad OC, Langer R (2012) Mass production and size control of lipid-polymer hybrid nanoparticles through controlled microvortices. Nano Lett 12:3587–3591
Lee J, Kwon S (2009) Mixing efficiency of a multilamination micromixer with consecutive recirculation zones. Chem Eng Sci 64:1223–1231
Lee MG, Choi S, Park JK (2010) Rapid multivortex mixing in an alternately formed contraction–expansion array microchannel. Biomed Microdevices 12:1019–1026
Lim DSW, Shelby JP, Kuo JS, Chiu DT (2003) Dynamic formation of ring-shaped patterns of colloidal particles in microfluidic systems. App Phys Lett 83(6):1145–1147
Lin G, Makarov D, Schmidt OG (2017) Magnetic sensing platform technologies for biomedical applications. Lab Chip 17(11):1884–1912
Lindken R, Rossi M, Große S, Westerweel J (2009) Micro-particle image velocimetry (μPIV): recent developments, applications, and guidelines. Lab Chip 9:2551–2567
Lindström S, Andersson-Svahn H (2010) Overview of single-cell analyses: microdevices and applications. Lab Chip 10:3363–3372
Liu K, Pitchimani R, Dang D, Bayer K, Harrington T, Pappas D (2008) Cell culture chip using low-shear mass transport. Langmuir 24:5955–5960
Luo C, Zhu X, Yu T, Luo X, Ouyang Q, Ji H, Chen Y (2008) A fast cell loading and high-throughput microfluidic system for long-term cell culture in zero-flow environments. Biotechnol Bioeng 101:190–195
Mach AJ, Kim JH, Arshi A, Hur SC, Di Carlo D (2011) Automated cellular sample preparation using a centrifuge-on-a-chip. Lab Chip 11:2827–2834
Marchalot J, Fouillet Y, Achard JL (2014) Multi-step microfluidic system for blood plasma separation: architecture and separation efficiency. Microfluid Nanofluid 17:167–180
Mu X, Zheng WF, Sun JS, Zhang W, Jiang XY (2013) Microfluidics for manipulating cells. Small 9(1):9–21
Niu X, Gielen F, Edel JB, Demello AJ (2011) A microdroplet dilutor for high-throughput screening. Nat Chem 3(6):437–442
Oysterman N, Derganc J, Svenšek D (2016) Formation of vortices in long microcavities at low Reynolds number. Microfluid Nanofluid. https://doi.org/10.1007/s10404-015-1689-7
Park JS, Song SH, Jung HI (2009) Continuous focusing of microparticles using inertial lift force and vorticity via multi-orifice microfluidic channels. Lab Chip 9(7):939–948
Park JY, Morgan M, Sachs AN, Samorezov J, Teller R, Shen Y, Pienta KJ, Takayama S (2010) Single cell trapping in larger microwells capable of supporting cell spreading and proliferation. Microfluid Nanofluid 8:263–268
Pertaya-Braun N, Baier T, Hardt S (2011) Microfluidic centrifuge based on a counterflow configuration. Microfluid Nanofluid 12:317–324
Petit T, Zhang L, Peyer KE, Kratochvil BE, Nelson BJ (2012) Selective trapping and manipulation of microscale objects using mobile microvortices. Nano Lett 12:156–160
Raffel M, Willert CE, Wereley ST, Kompenhans J (2007) Particle image velocimetry—a practical guide, 2nd edn. Springer-Verlag, Berlin
Romero-Mendez R, Yang KT, McClain R (1999) Effect of fin spacing on convection in a plate fin and tube heat exchanger. Int J Heat Mass Transfer 43:39–51
Sackmann EK, Fulton AL, Beebe DJ (2014) The present and future role of microfluidics in biomedical research. Nature 507(7491):181–189
Sajeesh P, Sen AK (2014) Particle separation and sorting in microfluidic devices: a review. Microfluid Nanofluid 17(1):1–52
Shah RK, London AL (1978) Laminar flow forced convection in ducts. Academic Press, New York
Shankar PN (1997) Three-dimensional eddy structure in a cylindrical container. J Fluid Mech 342:97–118
Shankar PN, Deshpande MD (2000) Fluid mechanics in the driven cavity. Annu Rev Fluid Mech 32:93–136
Shelby JP, Lim DSW, Kuo JS, Chiu DT (2003) Microfluidic systems: high radial acceleration in microvortices. Nature 425:38
Shelby JP, Mutch SA, Chiu DT (2004) Direct manipulation and observation of the rotational motion of single optically trapped microparticles and biological cells in microvortices. Anal Chem 76(9):2492–2497
Shen C, Floryan JM (1985) Low Reynolds number flow over cavities. Phys Fluids 28:3191–3202
Shen F, Xiao P, Liu Z (2015) Microparticle image velocimetry (μPIV) study of microcavity flow at low Reynolds number. Microfluid Nanofluid 19:403–417
Shen F, Li Y, Wang G, Liu Z (2017a) Mechanisms of rectangular groove-induced multiple-microdroplet coalescences. Acta Mech Sin 33(3):585–594
Shen F, Xu M, Wang Z, Liu Z (2017b) Single-particle trapping, orbiting, and rotating in a microcavity using microfluidics. Appl Phys Express 10:097301
Shih TR, Chung CK (2007) A high-efficiency planar micromixer with convection and diffusion mixing over a wide Reynolds number range. Microfluid Nanofluid 5:175–183
Skelley AM, Kirak O, Suh H, Jaenisch R, Voldman J (2009) Microfluidic control of cell pairing and fusion. Nat Methods 6:147–152
Sollier E, Cubizolles M, Fouillet Y, Achard JL (2010) Fast and continuous plasma extraction from whole human blood based

on expanding cell-free layer devices. Biomed Microdevices 12:485–497
Sollier E, Go DE, Che J, Gossett DR, O'Byrne S, Weaver WM, Kummer N, Rettig M et al (2014) Size-selective collection of circulating tumor cells using vortex technology. Lab Chip 14:63–77
Stone HA, Stroock AD, Ajdari A (2004) Engineering flows in small devices: microfluidics toward a lab-on-a-chip. Annu Rev Fluid Mech 36(1):381–411
Tan YC, Fisher JS, Lee AI, Cristini V, Lee AP (2004) Design of microfluidic channel geometries for the control of droplet volume, chemical concentration, and sorting. Lab Chip 4:292–298
Tenenbaumkatan J, Fishler R, Rothenrutishauser B, Sznitman J (2015) Biomimetics of fetal alveolar flow phenomena using microfluidics. Biomicrofluidics 9(1):91–114
Utada AS, Lorenceau E, Link DR, Kaplan PD, Stone HA, Weitz DA (2005) Monodisperse double emulsions generated from a microcapillary device. Science 308:537–541
Vrhovec S, Kavcic B, Mally M, Derganc J (2011) A microfluidic diffusion chamber for reversible environmental changes around flaccid lipid vesicles. Lab Chip 11:4200–4206
Wang W, Yang C, Li CM (2009) On-demand microfluidic droplet trapping and fusion for on-chip static droplet assays. Lab Chip 9(11):1504–1506
Wang X, Zhou J, Papautsky I (2013) Vortex-aided inertial microfluidic device for continuous particle separation with high size-selectivity, efficiency, and purity. Biomicrofluidics 7:044119
Wereley ST, Meinhart CD (2010) Recent advances in micro-particle image velocimetry. Annu Rev Fluid Mech 42:557–576
Whitesides GM (2006) The origins and the future of microfluidics. Nature 442(7101):368–373
Williams SJ, Park C, Wereley ST (2010) Advances and applications on microfluidic velocimetry techniques. Microfluid Nanofluid 8:709–726
Yew AG, Pinero D, Hsieh AH, Atencia J (2013) Low Peclet number mass and momentum transport in microcavities. Appl Phys Lett 102:084108
Yu ZTF, Lee YK, Wong M, Zohar Y (2005) Fluid flows in microchannels with cavities. J Microelectromech Syst 14:1386–1398
Zhang J, Yan S, Yuan D, Alici G, Nguyen N-T, Ebrahimi Warkiani M, Li W (2016) Fundamentals and applications of inertial microfluidics: a review. Lab Chip 16(1):10–34
Zhou J, Kasper S, Papautsky I (2013) Enhanced size-dependent trapping of particles using microvortices. Microfluid Nanofluid 15:611–623